


# Structural Properties and Reactivity Trends of Molybdenum Oxide Catalysts Supported on Zirconia for the Hydrodeoxygenation of Anisole

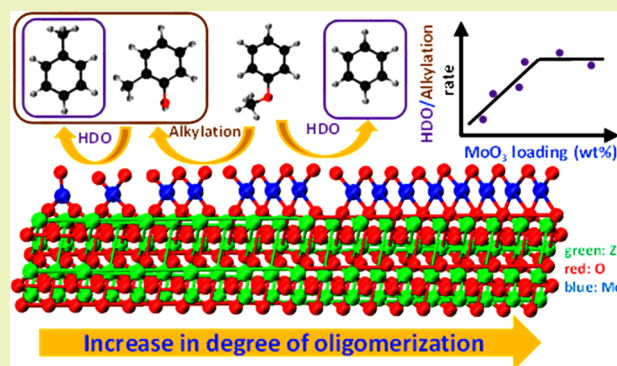
Manish Shetty, Karthick Murugappan, William H. Green, and Yuriy Román-Leshkov\*

Department of Chemical Engineering, Massachusetts Institute of Technology, Cambridge, Massachusetts 02139, United States

 Supporting Information

**ABSTRACT:** Vapor-phase hydrodeoxygenation (HDO) of anisole was investigated at 593 K and H<sub>2</sub> pressures of  $\leq 1$  bar over supported MoO<sub>3</sub>/ZrO<sub>2</sub> catalysts with MoO<sub>3</sub> loadings ranging from 1 to 36 wt % (i.e., 0.5–23.8 Mo/nm<sup>2</sup>). Reactivity studies showed that HDO activity increased proportionally with MoO<sub>3</sub> coverage up to a monolayer coverage ( $\sim 15$  wt %) over the ZrO<sub>2</sub> surface. Specific rates declined for catalysts with high loadings exceeding the monolayer coverage, because of a decreasing amount of redox-active species, as confirmed by oxygen chemisorption experiments. For low catalyst loadings (1 and 5 wt %), the selectivities toward fully deoxygenated aromatics were 13 and 24% on a C-mol basis, respectively, while at intermediate and high loadings (10–36 wt %), the selectivity was  $\sim 40\%$ . Post-reaction characterization of the spent catalysts using X-ray diffraction and X-ray photoelectron spectroscopy showed that the catalysts with 25 and 36 wt % MoO<sub>3</sub> loadings were over-reduced, as evidenced by the prevalence of Mo<sup>4+</sup> and Mo<sup>3+</sup> oxidation states summing to 54 and 67%, respectively. In contrast, catalysts with low and intermediate Mo loadings exhibited a prevalence of Mo<sup>6+</sup> species ( $\sim 60\%$ ). We hypothesize that Mo<sup>5+</sup> species are more easily stabilized in oligomeric and isolated forms over the zirconia support. The catalysts with intermediate loadings feature HDO and alkylation rates higher than those of catalysts with low loadings because the latter feature a higher proportion of isolated species. Once the monolayer coverage is exceeded, MoO<sub>3</sub> crystallites are formed, which can undergo facile reduction to less reactive MoO<sub>2</sub>.

**KEYWORDS:** Hydrodeoxygenation (HDO), Lignin-derived oxygenates, Anisole HDO, Supported molybdenum oxides, Oligomeric dispersion, Biomass conversion



## INTRODUCTION

Catalytic fast pyrolysis (CFP) is an attractive technology for valorizing biomass into transportation fuels and value-added chemicals.<sup>1–4</sup> Conventional hydrotreatment catalysts such as CoMo- and NiMo-based sulfides and supported base and noble metal catalysts have been reported to produce energy-dense, stable, and valorized products from pyrolysis oils and lignin monomers and dimers obtained from the catalytic reductive fractionation of biomass.<sup>2,5–15</sup> However, they require high H<sub>2</sub> pressures that lead to aromatic ring hydrogenation, resulting in products with a low octane number and an increased level of H<sub>2</sub> consumption.<sup>2</sup> Zeolites are the state-of-the-art catalysts for CFP,<sup>16,17</sup> but their performance is limited by the inherently hydrogen poor nature of lignocellulosic biomass, which results in a high level of coke formation.<sup>18,19</sup> Recently, Román-Leshkov and co-workers demonstrated that bulk and supported MoO<sub>3</sub> are effective hydrodeoxygenation (HDO) catalysts capable of selectively cleaving C–O bonds in various bio-derived model oxygenates to produce olefinic and aromatic hydrocarbons under mild conditions (593 K and H<sub>2</sub> partial pressures of  $\leq 1$

bar).<sup>20–22</sup> Importantly, MoO<sub>3</sub>-based catalysts were shown to be effective for the CFP of lignocellulosic biomass.<sup>23–26</sup> When the genesis of the catalytic activity of these materials was being rationalized, it was hypothesized that HDO occurs via an oxygen vacancy-driven mechanism promoted by undercoordinated Mo<sup>5+</sup> species. Indeed, a higher prevalence of Mo<sup>5+</sup> species was observed when MoO<sub>3</sub> oligomers were dispersed over large-surface area TiO<sub>2</sub> and ZrO<sub>2</sub> supports at a loading of 10 wt %. Furthermore, the supports prevent the over-reduction of these MoO<sub>3</sub> oligomers.<sup>22,24</sup>

Although the nature of dispersed MoO<sub>x</sub> species has been shown to impact activity and selectivity in other reactions, including methanol oxidation, oxidative dehydrogenation (ODH) of propane, and selective oxidation of dimethyl ether to formaldehyde,<sup>27–29</sup> to the best of our knowledge, no systematic studies have been conducted to investigate the effect

Received: March 1, 2017

Revised: March 27, 2017

Published: April 5, 2017

of MoO<sub>x</sub> dispersion on HDO reactions. Here, we investigate the influence of MoO<sub>3</sub> dispersion over a ZrO<sub>2</sub> support on anisole HDO rates. Supported catalysts with MoO<sub>3</sub> loadings ranging from 1 to 36 wt % were synthesized, with the objective of creating controlled amounts of isolated, oligomeric species, and crystalline MoO<sub>3</sub> and Zr(MoO<sub>4</sub>)<sub>2</sub> crystallites. The origin of the observed differences in HDO rates as a function of MoO<sub>x</sub> loading was investigated by combining reactivity studies with characterization techniques such as hydrogen temperature-programmed reduction (H<sub>2</sub>-TPR), Raman spectroscopy, oxygen chemisorption, and X-ray photoelectron spectroscopy (XPS).

## EXPERIMENTAL SECTION

All catalysts were prepared using a wet impregnation method described in detail in the [Supporting Information](#). Catalytic activity and stability experiments were performed in a vapor-phase packed-bed down-flow reactor. The reactor consisted of a stainless steel tube (0.95 cm outside diameter) with a wall thickness of 0.089 cm mounted in a single-zone furnace (Applied Test Systems, Series 3210, 850 W and 115 V). The temperature was controlled by a temperature controller (Digi-Sense, model 68900-10) connected to a K-type thermocouple (Omega, model TJ36-CAXL-116u) mounted downstream in direct contact with the catalyst bed. Except for 1 wt % MoO<sub>3</sub>/ZrO<sub>2</sub>, all catalysts were pelletized between 100 and 140 mesh, mixed with an inert α-Al<sub>2</sub>O<sub>3</sub> diluent (total 1 g), and packed between two layers of α-Al<sub>2</sub>O<sub>3</sub> (1.5 g each) in the middle of the furnace. For the 1 wt % MoO<sub>3</sub>/ZrO<sub>2</sub> sample, the catalyst (2.5 g) was mixed with 1.5 g of the inert diluent. The total volume of the bed was ~2 cm<sup>3</sup>. Prior to reaction, the reactor temperature was ramped at a rate of ~6 K min<sup>-1</sup> under N<sub>2</sub> until reaching a reaction temperature of 593 K. Next, anisole was delivered into the reactor via a capillary tube (U-117, IDEX Health) connected to a syringe pump (Harvard Apparatus, model 70300S) and mixed with H<sub>2</sub> gas at the inlet of the reactor. Flow rates were adjusted to obtain a weight hourly space velocity (WHSV) of 7.96 h<sup>-1</sup>, defined with respect to an equivalent mass of MoO<sub>3</sub> loaded ([eq 1](#)). The mass of equivalent MoO<sub>3</sub> was computed as the product of MoO<sub>3</sub> loading and total loaded mass of the catalyst.

$$\text{WHSV (h}^{-1}\text{)} = \frac{\text{mass flow rate of reactant fed}}{\text{mass of equivalent MoO}_3 \text{ loaded}} \quad (1)$$

The reactor effluent lines were heated to 523 K to prevent condensation. The effluents were analyzed and quantified via an online gas chromatograph (GC) equipped with a mass selective detector for identification (Agilent Technologies, model 5975 C) and a flame ionization detector for quantification (Agilent Technologies, model 7890 A). The GC was fitted with a DB-5 column [Agilent, 30 m × 0.25 mm (inside diameter) × 0.25 μm]. The following GC parameters were used for analysis: detector temperature of 573 K, injector temperature of 548 K, and split ratio of 1:20. The initial and final oven temperatures were 323 and 523 K, respectively, with a ramp of 10 K min<sup>-1</sup>.

The following equations were used to quantify experimental data:

$$\begin{aligned} \text{conversion (C-mol \%)} \\ &= \frac{\text{carbon moles of reactant consumed}}{\text{carbon moles of reactant fed}} \times 100 \end{aligned} \quad (2)$$

$$\begin{aligned} \text{selectivity (C-mol \%)} \\ &= \frac{\text{carbon moles in product}}{\text{carbon moles of reactant consumed}} \times 100 \end{aligned} \quad (3)$$

$$\text{yield (C-mol \%)} = \frac{\text{carbon moles in product}}{\text{carbon moles of reactant fed}} \times 100 \quad (4)$$

$$\begin{aligned} \text{specific HDO reaction rate [mmol of C h}^{-1} \text{ (g of MoO}_3\text{)}^{-1}\text{]} \\ &= (\text{molar carbon flow rate of HDO products formed}) \\ &/ (\text{equivalent mass of MoO}_3 \text{ loaded}) \end{aligned} \quad (5)$$

$$\begin{aligned} \text{specific alkylation reaction rate [mmol of C h}^{-1} \text{ (g of catalyst)}^{-1}\text{]} \\ &= (\text{molar carbon flow rate of alkylation products}) \\ &/ (\text{total mass of catalyst}) \end{aligned} \quad (6)$$

The HDO products refer to benzene, toluene, and other alkylated deoxygenated aromatics, while the alkylation products refer to alkylated deoxygenated aromatics, including toluene, alkylated phenols, including cresols, and alkylated anisoles, including methyl anisole.

Surface area measurements and oxygen chemisorption experiments were performed on a Quantachrome Autosorb iQ automated gas sorption system. The surface area was determined using nitrogen adsorption-desorption experiments at liquid nitrogen temperature (77 K) using the Brunauer-Emmett-Teller (BET) theory.<sup>30</sup> Mo density was calculated from the MoO<sub>3</sub> loading and the BET surface area as shown in [eq 7](#):

$$\begin{aligned} \text{Mo density (Mo /nm}^2\text{)} &= [\text{MoO}_3 \text{ loading (\%)}] \\ &/ [144 \times \text{BET surface area (m}^2\text{/g)}] \times 6.023 \times 10^3 \end{aligned} \quad (7)$$

Oxygen chemisorption was performed on catalyst samples at 303 K. The samples were treated under He at 393 K for 0.5 h and then reduced in a flow of H<sub>2</sub> for 2 h at 623 K. The chemisorption cell was then evacuated under vacuum for 2 h prior to oxygen adsorption. A seven-point adsorption isotherm was measured at O<sub>2</sub> pressures between 80 and 560 mmHg. After first adsorption, weakly adsorbed O<sub>2</sub> was removed by degassing, and the adsorption isotherm was recorded again. The difference between the first and second isotherms was plotted and extrapolated to zero pressure to determine the amount of irreversibly adsorbed O<sub>2</sub>. The oxygen chemisorption data were used to quantify redox-active Mo species using [eqs 8 and 9](#). The uptake of oxygen from ZrO<sub>2</sub> was subtracted from the uptake of oxygen of the supported catalyst to determine the uptake from the Mo species. The rates of HDO were calculated from the measured redox-active Mo species on a carbon-mole basis, as shown below.

$$\begin{aligned} \text{moles of redox-active Mo species} \\ &= 2 \times \text{oxygen uptake (mol/g)} \times \text{catalyst mass (g)} \end{aligned} \quad (8)$$

$$\begin{aligned} \text{redox-active Mo species (\%)} \\ &= \frac{2 \times \text{oxygen uptake (mol/g)}}{\text{Mo loading (mol/g)}} \times 100 \end{aligned} \quad (9)$$

$$\begin{aligned} \text{rate of HDO (h}^{-1}\text{)} \\ &= \frac{\text{molar carbon flow rate of HDO products formed}}{\text{moles of redox-active Mo species}} \end{aligned} \quad (10)$$

All the characterization techniques are further detailed in the [Supporting Information](#).

## RESULTS

**Pre-Reaction Catalyst Characterization.** ICP-MS and powder X-ray diffraction (PXRD) were used to determine the loading and the phase of dispersed molybdenum on the ZrO<sub>2</sub> support. ICP-MS analysis confirmed the loading of MoO<sub>3</sub> on the supported catalysts to be close to the theoretical loading. PXRD patterns for ZrO<sub>2</sub> and MoO<sub>3</sub>/ZrO<sub>2</sub> catalysts are shown in [Figure 1](#). Bulk ZrO<sub>2</sub> was present as a mixture of monoclinic and tetragonal phases. Dispersed MoO<sub>x</sub> species are known to prevent the transformation of the tetragonal phase to the

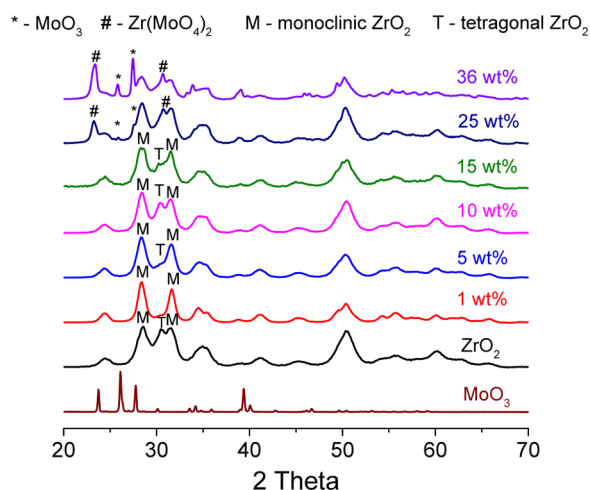


**Figure 1.** Powder X-ray diffraction (PXRD) patterns of MoO<sub>3</sub>, ZrO<sub>2</sub>, and 1–36 wt % supported MoO<sub>3</sub>/ZrO<sub>2</sub> catalysts normalized by the maximal peak intensity of each catalyst.

monoclinic phase of ZrO<sub>2</sub> during calcination.<sup>31–33</sup> Hence, we observed a progressive increase in the level of formation of tetragonal ZrO<sub>2</sub> on the post-calcined catalysts up to a loading of 15 wt %. At high loadings (25 and 36 wt %), the phase composition of the support could not be determined because of overlap of the tetragonal phase and Zr(MoO<sub>4</sub>)<sub>2</sub> diffractions. With the exception of 25 and 36 wt % MoO<sub>3</sub>/ZrO<sub>2</sub>, which exhibited the presence of both MoO<sub>3</sub> and Zr(MoO<sub>4</sub>)<sub>2</sub> crystallites, low- and intermediate-loading catalysts did not show the presence of any MoO<sub>3</sub> and Zr(MoO<sub>4</sub>)<sub>2</sub> crystallites.

Raman spectroscopy was used to probe vibrational modes of Mo–O bonds (Figure 2). The antisymmetric (Mo–O–Mo)

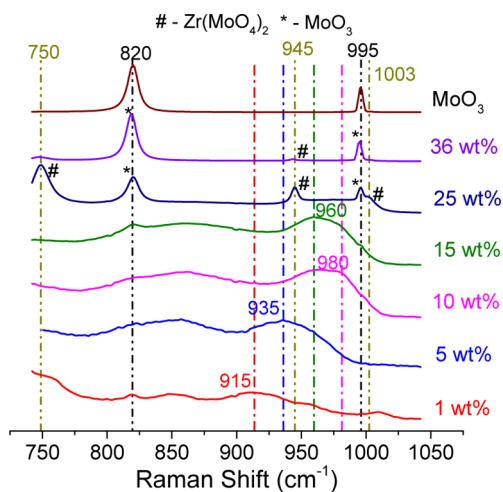


**Figure 2.** Raman spectra of MoO<sub>3</sub> and 1–36 wt % supported MoO<sub>3</sub>/ZrO<sub>2</sub> catalysts in the Raman shift range of 725–1075 cm<sup>-1</sup> normalized by the maximal peak intensity of each catalyst.

and terminal (Mo=O) stretching modes provide information about the local structure of dispersed MoO<sub>x</sub> domains. The bands corresponding to terminal (Mo=O) stretching modes moved to higher Raman shifts with an increase in Mo loading, as evidenced by the shifting of the band at 915 cm<sup>-1</sup> for 1 wt % loading to 980 cm<sup>-1</sup> for 15 wt % loading. This shift suggests an increased level of oligomerization of MoO<sub>x</sub> domains as the loading approaches the monolayer coverage ( $\sim 5$  Mo/nm<sup>2</sup>) on

the support surface at higher Mo loadings.<sup>29,34–37</sup> In agreement with PXRD, catalysts at high loadings (25 and 36 wt %) exhibited bands corresponding to bulk MoO<sub>3</sub> (995 and 820 cm<sup>-1</sup>) and Zr(MoO<sub>4</sub>)<sub>2</sub> (750, 945, and 1003 cm<sup>-1</sup>) crystals. Additionally, while 36 wt % MoO<sub>3</sub>/ZrO<sub>2</sub> showed less intense bands corresponding to Zr(MoO<sub>4</sub>)<sub>2</sub>, the catalyst with 25 wt % loading exhibited bands corresponding to MoO<sub>3</sub> and Zr(MoO<sub>4</sub>)<sub>2</sub> with similar intensities. We note that bands corresponding to crystalline MoO<sub>3</sub> are present in the 15 wt % sample at a very low intensity, which is expected given that the Mo content is close to the theoretical monolayer coverage of 5 Mo/nm<sup>2</sup>.<sup>37</sup> However, because crystalline MoO<sub>3</sub> bands are 10–10<sup>3</sup> times more intense than both isolated and oligomeric species,<sup>34,38</sup> this relatively weak intensity for crystalline MoO<sub>3</sub> bands suggests that oligomeric MoO<sub>x</sub> domains are predominantly present on this sample. Overall, our Raman spectroscopic data show that the degree of oligomerization increases until a monolayer coverage ( $\sim 5$  Mo/nm<sup>2</sup>) of MoO<sub>x</sub> is reached, followed by the formation of stand-alone crystallites at higher loadings. The nature of dispersed MoO<sub>x</sub> species can thus be controlled by changing the MoO<sub>3</sub> loading on the ZrO<sub>2</sub> support in the sub-monolayer regime.

Diffuse reflectance ultraviolet–visible (DRUV) spectra was used to obtain absorption band gap energies of the supported catalysts. Absorption band gap energies provide useful information about the dispersion of MoO<sub>x</sub> species on the support surface. The absorption band gap energies for bulk ZrO<sub>2</sub> and MoO<sub>3</sub> were 5.2 and 3.1 eV, respectively. A progressive reduction in absorption band gap energies was observed on the supported catalysts from 5.1 eV for the 1 wt % sample to 3.6 eV for the 15 wt % sample, confirming the trend of an increasing degree of polymerization of MoO<sub>x</sub> domains on the support surface with an increasing loading (Figure S1).<sup>32,37</sup> For the 25 and 36 wt % MoO<sub>3</sub>/ZrO<sub>2</sub> catalysts, the absorption band gap energies were 3.5 and 3.6 eV, respectively. In agreement with previous reports, we observed that the absorption band gap energies plateau at  $\sim 3.5$  eV once the monolayer coverage is achieved.<sup>32</sup>

BET surface areas for the catalysts were used to characterize textural properties of the catalyst, as summarized in Table 1 and

**Table 1.** Textural Properties of ZrO<sub>2</sub> and 1–36 wt % MoO<sub>3</sub>/ZrO<sub>2</sub> Catalysts

catalyst loading (wt %)	BET surface area (m <sup>2</sup> /g)	Mo density (Mo/nm <sup>2</sup> )
0 <sup>a</sup>	142	0
1	86	0.5
5	116	1.8
10	112	3.7
15	125	5.0
25	90	11.7
36	63	23.8

<sup>a</sup>ZrO<sub>2</sub> support.

Figure S2. In general, the BET surface area increased from 86 m<sup>2</sup>/g (1 wt %) to 125 m<sup>2</sup>/g (15 wt %), because of the higher concentration of MoO<sub>x</sub> species that prevent the sintering of ZrO<sub>2</sub>.<sup>37</sup> At the highest loadings (25 and 36 wt %), the Mo density was higher than a monolayer coverage ( $\sim 5$  Mo/nm<sup>2</sup>)<sup>34</sup> and the surface area started to decrease because of the formation of MoO<sub>3</sub> and Zr(MoO<sub>4</sub>)<sub>2</sub> crystallites.

**Reactivity Studies Using MoO<sub>3</sub>/ZrO<sub>2</sub> Catalysts.** The product distributions obtained for all the supported catalysts

are reported in Figure 3 (TOS data given in Figure S3) at 593 K and a WHSV of  $7.96 \text{ h}^{-1}$ . On an equivalent  $\text{MoO}_3$  mass basis,

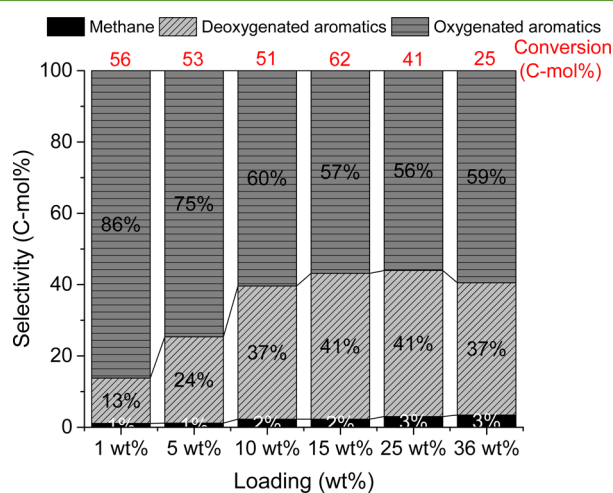


**Figure 3.** Reactivity data for 1–36 wt %  $\text{MoO}_3/\text{ZrO}_2$  catalysts for HDO of anisole. Reaction conditions:  $T = 593 \text{ K}$ ,  $P_{\text{total}} = 1.013 \text{ bar}$  ( $0.0098P_{\text{feed}}$ , balance  $\text{H}_2$ ), and  $\text{WHSV} = 7.96 \text{ h}^{-1}$ . 25 mg equivalent of  $\text{MoO}_3$ . The conversions and selectivities are averaged over a TOS of 0–4 h. Deoxygenated aromatics include benzene, toluene, and higher alkylated benzenes. Oxygenated aromatics include phenol, alkylated phenols, and alkylated anisoles. The detailed product distributions are given in Figure S4.

conversions for 1–15 wt %  $\text{MoO}_3/\text{ZrO}_2$  catalysts ranged from 51 to 62%. However, the selectivity toward deoxygenated products (i.e., benzene, toluene, and higher alkylated aromatic products) increased from 13 to 41% in proportion to the increase in loading, while the selectivity toward methane remained at  $\leq 4\%$  for all catalysts. The major oxygenated aromatic products were phenol, cresol (mainly *o*-cresol), methyl anisole, dimethyl phenol, and higher alkylated phenols. Figure S4 shows detailed product selectivities of the deoxygenated and oxygenated aromatics. Overall, benzene was the dominant deoxygenated aromatic product at all loadings. For the oxygenated aromatics, phenol and cresol were formed with the highest selectivity (18–32 and 16–34% for phenol and cresol, respectively, across all  $\text{MoO}_3$  loadings). At the highest loadings of 25 and 36 wt %, while the selectivities toward deoxygenated aromatics remained constant at  $\sim 40\%$ , the conversions decreased to 41 and 25%, respectively. The overall conversion rate was thus largely constant at loadings of  $\leq 15 \text{ wt } \%$ , followed by a reduction at loadings of 25 and 36 wt %. To compare the product distribution using the 36 wt %  $\text{MoO}_3$  catalyst at a conversion level similar to that obtained with the other catalysts ( $\sim 42\%$ ), an experiment with a longer space time (i.e., increased catalyst mass) was performed under otherwise identical conditions. The selectivity toward deoxygenated aromatics was  $\sim 46\%$  (Figure S5). Control experiments using  $\text{ZrO}_2$  showed no appreciable HDO activity for anisole (Figure S6), thereby confirming that the HDO reactivity arises from the Mo species. We note that  $\alpha\text{-Al}_2\text{O}_3$  without any catalyst showed a low conversion of  $\sim 4\%$  with a yield of  $\sim 2\%$  toward phenol, while the remaining products were methane, benzene, toluene, and methyl anisole. Overall, the results show that as the  $\text{MoO}_x$  coverage approaches a monolayer coverage, the selectivity toward deoxygenated aromatics approaches a constant value ( $\sim 40\%$ ). At coverages higher than a monolayer,

while the presence of crystalline species reduces the availability of Mo species, the activity of the available Mo species remains constant, as evidenced by the similar selectivity values for HDO products in spite of the lower conversion.

Oxygen chemisorption data were used to quantify the percent of redox-active Mo species for 1–36 wt %  $\text{MoO}_3$  samples (see Table 2). The percent of redox-active Mo species

**Table 2.** Oxygen Chemisorption Values for 1–36 wt %  $\text{MoO}_3/\text{ZrO}_2$  Catalysts at 303 K<sup>a</sup>

catalyst loading (wt %)	oxygen uptake ( $\mu\text{mol/g}$ )	% redox-active species
1	10	28
5	60	34
10	107	31
15	143	27
25	130	15
36	108	9

<sup>a</sup>Corrected for uptake of  $\text{O}_2$  from  $\text{ZrO}_2$ . The temperature of reduction was 623 K.

ranged between 27 and 34% for loadings between 1 and 15 wt %. These results indicate a similar level of redox-active Mo sites at loadings lower than a monolayer. At  $\text{MoO}_3$  loadings of 25 and 36 wt %, the percent of redox-active species decreased to 15 and 9%, respectively. The formation of crystalline  $\text{MoO}_3$  species reduces the availability of reactive species for redox reactions,<sup>39–41</sup> as manifested by the decrease in the number of redox-active Mo species. As seen in Figure 4a, for sub-monolayer coverages, the specific HDO reaction rate increased linearly to a monolayer coverage, followed by a linear decrease in activity for the highest loadings (25 and 36 wt %). Notably, upon normalization of the rates by oxygen uptake, a linear increase is observed up to the monolayer coverage limit (Figure 4b), beyond which a constant HDO rate is attained, thereby suggesting that the decrease in the specific HDO rate at high loadings is due to the decrease in the number of active Mo species. Even with the higher catalyst mass for 36 wt %  $\text{MoO}_3/\text{ZrO}_2$ , both the specific HDO reaction rate and the rate of HDO were similar (Figure S5). Further, these data suggest that in the sub-monolayer range, the lower reactivity observed at the lowest loadings (1 and 5 wt %) may be due to a difference in the nature of dispersed  $\text{MoO}_x$  species. Note that the higher activity observed with an increasing  $\text{MoO}_3$  loading appears to be correlated with the increase in the degree of oligomerization of  $\text{MoO}_x$  species detected using Raman spectroscopy (*vide supra*).

Alkylation rates of the catalysts as a function of  $\text{MoO}_3$  loading are shown in Figure 5. The rate of alkylation increased from 1.8 to  $27.3 \text{ mmol of C h}^{-1} (\text{g of catalyst})^{-1}$  until a monolayer coverage was reached ( $\sim 15 \text{ wt } \%$  loading). After a monolayer coverage is achieved, the rate of alkylation decreased to  $21.7 \text{ mmol of C h}^{-1} (\text{g of catalyst})^{-1}$  at 36 wt % loading. The formation of alkylated oxygenated and deoxygenated aromatics, including toluene, cresol, and dimethyl phenol, occurs because of both intra- and intermolecular alkylation. As seen in Figure S6,  $\text{ZrO}_2$  was inactive for HDO; however, it formed alkylated oxygenated aromatics, including methyl anisole and *o*-cresol. Hence, both the Mo species and the support are active for alkylation.  $\text{ZrO}_2$  exhibited a specific alkylation rate of  $5.0 \text{ mmol of C h}^{-1} (\text{g of catalyst})^{-1}$ . We note that this initial decrease from 5.0 to  $1.8 \text{ mmol of C h}^{-1} (\text{g of catalyst})^{-1}$  after the incorporation of 1 wt %  $\text{MoO}_3$  on  $\text{ZrO}_2$  occurs due to a

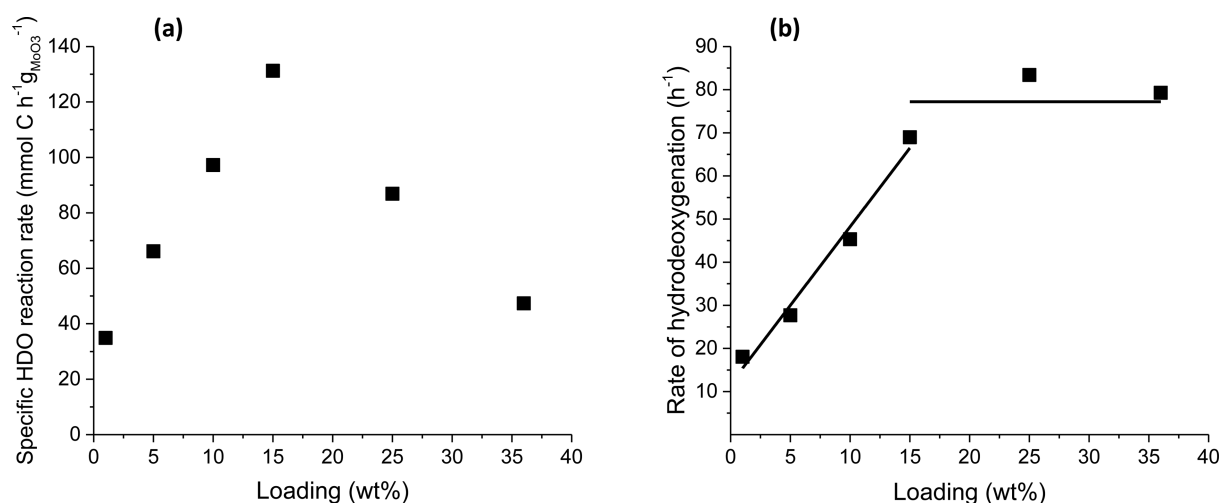


**Figure 4.** Hydrodeoxygenation (HDO) reaction rate data for 1–36 wt % MoO<sub>3</sub>/ZrO<sub>2</sub> for HDO of anisole. (a) Specific HDO reaction rate normalized by the equivalent mass of MoO<sub>3</sub>. (b) Rate of HDO normalized by percent redox-active Mo species obtained from oxygen chemisorption experiments. Reaction conditions:  $T = 593$  K,  $P_{\text{total}} = 1.013$  bar ( $0.0098P_{\text{feed}}$  balance H<sub>2</sub>), and  $\text{WHSV} = 7.96$  h<sup>-1</sup>. 25 mg equivalent of MoO<sub>3</sub>. Reactivity data were calculated by averaging the reaction rate data collected over a TOS period of 0–4 h.

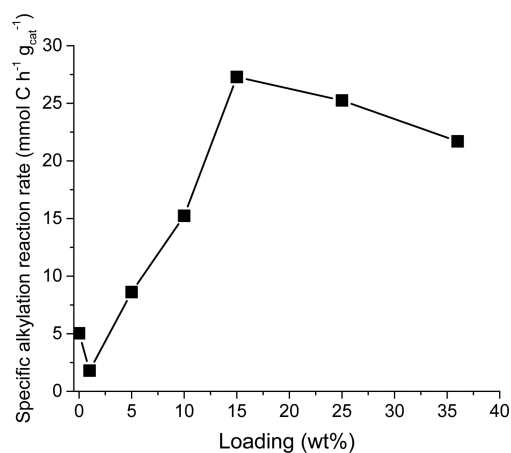


**Figure 5.** Specific alkylation reaction rates for 1–36 wt % MoO<sub>3</sub>/ZrO<sub>2</sub> for the HDO of anisole. Reaction conditions:  $T = 593$  K,  $P_{\text{total}} = 1.013$  bar ( $0.0098P_{\text{feed}}$  balance H<sub>2</sub>), and  $\text{WHSV} = 7.96$  h<sup>-1</sup>. 25 mg equivalent of MoO<sub>3</sub>. The conversions and selectivities are averaged over a TOS of 0–4 h.

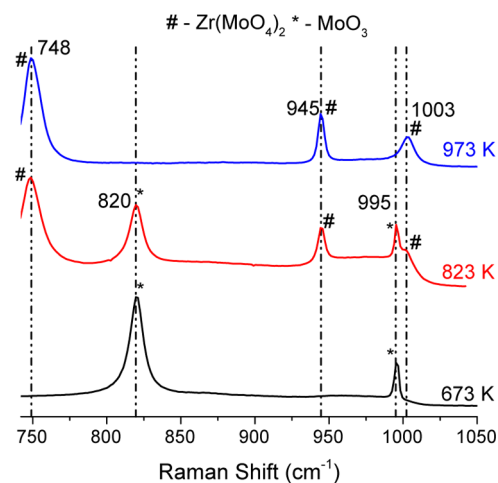


**Figure 6.** Normalized Raman spectra of 25 wt % MoO<sub>3</sub>/ZrO<sub>2</sub> catalysts calcined at 673, 823, and 973 K. Data are shown in the Raman shift range of 745–1050 cm<sup>-1</sup> and normalized by the maximal peak intensity of each catalyst.

decreased number of alkylation sites on the support in exchange for additional HDO sites coming from MoO<sub>3</sub>. In addition, the rate of alkylation was similar for 36 wt % MoO<sub>3</sub>/ZrO<sub>2</sub> at the two different catalyst masses (Figure S5).

The impact of the molybdenum phase on the reactivity was studied on 25 wt % MoO<sub>3</sub>/ZrO<sub>2</sub>. 25 wt % MoO<sub>3</sub>/ZrO<sub>2</sub> calcined at 673 and 973 K selectively formed MoO<sub>3</sub> and Zr(MoO<sub>4</sub>)<sub>2</sub> crystallites, respectively (Figure 6), as compared to the formation of a mixture of MoO<sub>3</sub> and Zr(MoO<sub>4</sub>)<sub>2</sub> crystallites at a calcination temperature of 823 K (Figures 1 and 2). The product distribution for the 25 wt % MoO<sub>3</sub>/ZrO<sub>2</sub> catalysts, as shown in Figure 7, shows that the selectivity toward deoxygenated products was ~40%, irrespective of the temperature of calcination. The detailed product distributions are given in Figure S7. The conversions were 42 and 41% for 25 wt % MoO<sub>3</sub>/ZrO<sub>2</sub> calcined at 673 and 823 K, respectively. However, the conversion decreased to 28% for the catalyst calcined at 973 K. The lower conversion seen for the catalyst calcined at 973 K can be rationalized to be due to the reduction

of the availability of redox-active MoO<sub>x</sub> species as seen in Table 3 (11% for a calcination temperature of 973 K as compared to 15–20% for calcination temperatures of 673 and 823 K).

**H<sub>2</sub> Temperature-Programmed Reduction (TPR) of Supported MoO<sub>3</sub>/ZrO<sub>2</sub> Catalysts.** The impact of speciation of MoO<sub>x</sub> species on the reducibility of supported catalysts was investigated by H<sub>2</sub>-TPR (see Figure 8). The observed maximal temperature of hydrogen consumption ( $T_{\text{max}}$ ) for the supported catalysts can be attributed to the reduction of dispersed Mo<sup>6+</sup> species to reduced states.<sup>41,42</sup> We note that our previous study established that the ZrO<sub>2</sub> support does not show any appreciable H<sub>2</sub> consumption in the range of 573–873 K.<sup>22</sup> Catalysts with low loadings (1 and 5 wt %) exhibited  $T_{\text{max}}$  values higher than those of intermediate- and high-Mo loading catalysts ( $\geq 10$  wt %). Specifically, 10, 15, 25, and 36 wt % MoO<sub>3</sub>/ZrO<sub>2</sub> featured  $T_{\text{max}}$  values of 710, 700, 785, and 760 K, with shoulders at 605, 620, 635, and 625 K, respectively. On the other hand, 1 and 5 wt % catalysts have higher  $T_{\text{max}}$  values of ~800 and ~720 K, respectively, with only 5 wt % catalyst

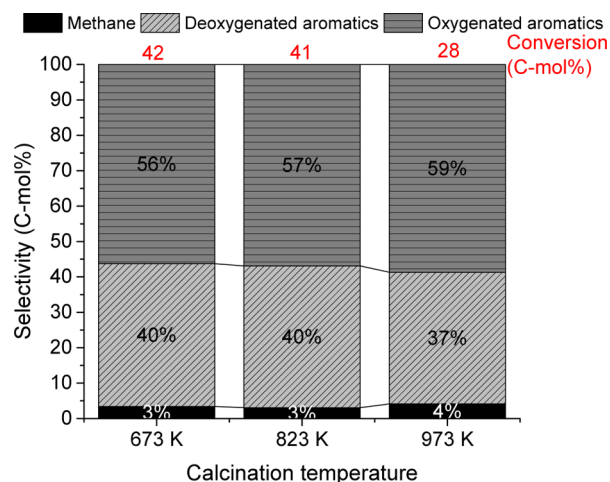


**Figure 7.** Selectivity and conversion values for anisole HDO using 25 wt % MoO<sub>3</sub>/ZrO<sub>2</sub> catalysts calcined at 673, 823, and 973 K. Reaction conditions:  $T = 593$  K,  $P_{\text{total}} = 1.013$  bar ( $0.0098P_{\text{feed}}$  balance H<sub>2</sub>), and WHSV = 7.96 h<sup>-1</sup>. 25 mg equivalent of MoO<sub>3</sub>. The conversions and selectivities are averaged over a TOS of 0–4 h. The detailed product distributions are shown in Figure S7.

**Table 3. Oxygen Chemisorption Values for 25 wt % MoO<sub>3</sub>/ZrO<sub>2</sub> Catalysts at a Chemisorption Temperature of 303 K<sup>a</sup>**

calcination temperature (K)	BET surface area (m <sup>2</sup> /g)	% redox-active species
673	87	20
823	90	15
973	52	11

<sup>a</sup>Corrected for uptake of O<sub>2</sub> from ZrO<sub>2</sub>. The temperature of reduction was 623 K.

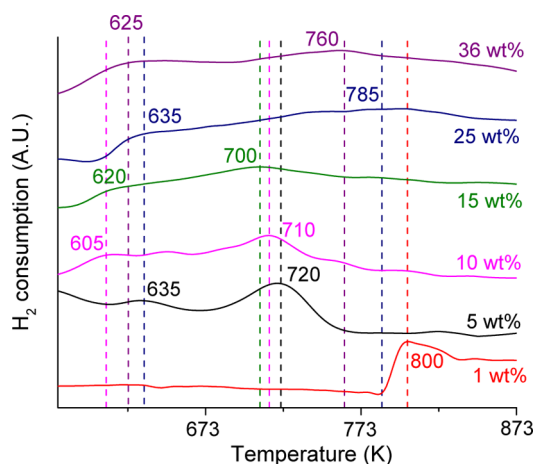


**Figure 8.** Hydrogen consumption during temperature-programmed reduction (TPR) of 1–36 wt % MoO<sub>3</sub>/ZrO<sub>2</sub> catalysts. Calcination with O<sub>2</sub> at 773 K for 2 h. TPR conditions: 1% H<sub>2</sub> flow rate = 50 mL min<sup>-1</sup> (20 mL min<sup>-1</sup> for 1 wt % MoO<sub>3</sub>/ZrO<sub>2</sub>), ramp = 5 K min<sup>-1</sup>. Masses of the supported catalyst of 25 mg equivalent MoO<sub>3</sub> for 5–36 wt % MoO<sub>3</sub>/ZrO<sub>2</sub> and 10 mg equivalent MoO<sub>3</sub> for 1 wt % MoO<sub>3</sub>/ZrO<sub>2</sub>.

exhibiting a shoulder at 635 K. These data show that low Mo loadings on ZrO<sub>2</sub> appear to decrease the reducibility of MoO<sub>3</sub> species. These observations are in agreement with previous reports showing that species populated at a low surface coverage of MoO<sub>x</sub> are more difficult to reduce.<sup>39</sup> The observed

initial decrease in  $T_{\text{max}}$  values followed by an increase with higher loadings has been demonstrated on supported MoO<sub>3</sub> and WO<sub>3</sub> catalysts in previous studies.<sup>28,40,41,43–48</sup>

**Post-Reaction PXRD and XPS Catalyst Characterization.** After reaction, appreciable structural changes were observed only for the high-loading catalysts, as evidenced by the differences in the PXRD patterns of the spent catalysts (Figure 9). The phase transformation of bulk MoO<sub>3</sub> and

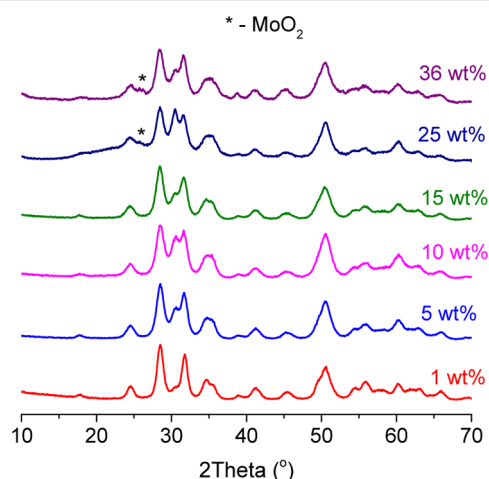


**Figure 9.** Normalized post-reaction powder X-ray diffraction (PXRD) patterns of 1–36 wt % MoO<sub>3</sub>/ZrO<sub>2</sub> spent catalysts. Reaction conditions:  $T = 593$  K,  $P_{\text{total}} = 1.013$  bar ( $0.0098P_{\text{feed}}$  balance H<sub>2</sub>), and WHSV = 7.96 h<sup>-1</sup>. TOS = 7 h. 25 mg equivalent of MoO<sub>3</sub>.

Zr(MoO<sub>4</sub>)<sub>2</sub> led to formation of MoO<sub>2</sub> for the catalysts with 25 and 36 wt % loadings. For loadings corresponding to a less than monolayer coverage ( $\leq 15$  wt %), no changes were observed in the PXRD patterns within the detection limit of the instrument ( $\sim 4$  nm).

XPS spectra were recorded on post-reaction samples to probe the final oxidation state of the surface Mo species (Figure 10) and to determine the extent of surface reduction. We note that the XPS spectra of all pre-reaction samples showed the

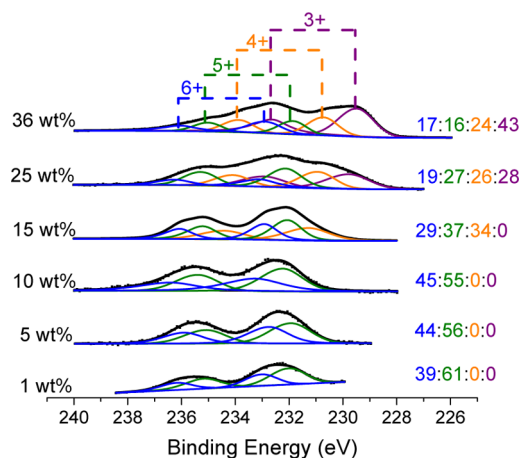


**Figure 10.** Normalized X-ray photoelectron spectra (XPS) of the Mo (3d) energy region of 1–36 wt % MoO<sub>3</sub>/ZrO<sub>2</sub> spent catalysts. The ratios displayed correspond to the proportion of oxidation states of Mo<sup>6+</sup>, Mo<sup>5+</sup>, Mo<sup>4+</sup>, and Mo<sup>3+</sup>. Reaction conditions:  $T = 593$  K,  $P_{\text{total}} = 1.013$  bar ( $0.0098P_{\text{feed}}$  balance H<sub>2</sub>), and WHSV = 7.96 h<sup>-1</sup>. TOS = 7 h. 25 mg equivalent of MoO<sub>3</sub>.

presence of only Mo<sup>6+</sup> species. However, reduced Mo species (Mo<sup>5+</sup>) were detected on all samples post-reaction. Deconvolution of the XPS peak areas shows that Mo<sup>5+</sup> oxidation states accounted for 61, 56, and 55% for the 1, 5, and 10 wt % samples, respectively, with the remaining species corresponding to Mo<sup>6+</sup>. Contrary to the presence of Mo<sup>4+</sup> species on post-reaction samples of 10 wt % MoO<sub>3</sub>/ZrO<sub>2</sub> for HDO of *m*-cresol to toluene,<sup>22</sup> no Mo<sup>4+</sup> was observed in our study. This result suggests that the degree of Mo reduction is likely feed-dependent. The 15 wt % sample showed 37% of Mo<sup>5+</sup> and 34% of Mo<sup>4+</sup> (remaining Mo<sup>6+</sup>). The 25 and 36 wt % samples had decreased levels of Mo<sup>5+</sup> (27 and 16%, respectively) with a concomitant increase in the levels of Mo<sup>3+</sup> (28 and 43%, respectively), based on the binding energy assignments by Choi and Thompson.<sup>49</sup> At these loadings, the larger amount of Mo<sup>4+</sup> and Mo<sup>3+</sup> states is consistent with the formation of MoO<sub>2</sub>. Furthermore, independent of the nature of dispersed MoO<sub>x</sub> species in the sub-monolayer dispersion, the catalysts exhibit a similar proportion of Mo<sup>5+</sup> species. For loadings lower than a monolayer (≤15 wt %), our results show that the support prevents the over-reduction of Mo<sup>6+</sup> species. At loadings greater than a monolayer, the over-reduction cannot be prevented, concomitant with crystalline MoO<sub>2</sub> formation.

## DISCUSSION

A number of studies have reported that the nature of MoO<sub>x</sub> species on the support surface is influenced by the loading of MoO<sub>3</sub>.<sup>29,32,36,39,41,50</sup> At very low loadings, isolated MoO<sub>x</sub> species are known to form on the support surface,<sup>31,35,41</sup> while at higher loadings, as the Mo density increases, isolated species condense to form oligomeric MoO<sub>x</sub> domains on the support surface.<sup>35,37</sup> The type of MoO<sub>x</sub> species is important for HDO given that isolated MoO<sub>x</sub> species have been reported to be less reducible than oligomeric MoO<sub>x</sub> species.<sup>39</sup> Our H<sub>2</sub>-TPR data indicated a trend of decreasing *T*<sub>max</sub> values with increasing MoO<sub>3</sub> loadings up to the limit of monolayer coverage. We hypothesize that while the numbers of undercoordinated Mo species are similar across all sub-monolayer loadings (as measured by oxygen chemisorption), the larger amounts of isolated MoO<sub>x</sub> domains at the lowest loadings of 1 and 5 wt % (as observed by Raman spectroscopy) translate to lower HDO rates. Furthermore, the acidity of MoO<sub>3</sub>/ZrO<sub>2</sub> catalysts has been reported to increase with higher loadings up to the monolayer coverage limit.<sup>41</sup> Theoretical and experimental investigations have indicated the presence of strong Brønsted acid sites on reducible metal oxide-supported catalysts, including MoO<sub>3</sub>/ZrO<sub>2</sub>. These studies related this strong acidity to the presence of oligomeric species, their ability to delocalize charge across multiple oxygen atoms, and their better accessibility and reducibility.<sup>43,44,51–54</sup> At loadings higher than a monolayer, the lower accessibility of oligomeric domains reduces their acidity. Hence, the acidity increases until a monolayer coverage and decreases upon formation of crystallites, which mirror the trend seen for *o*-xylene isomerization,<sup>43,44</sup> and alcohol dehydration reactions,<sup>32,50,53,55</sup> catalyzed by acid sites. Alkylation reactions are typically catalyzed by Brønsted acid sites<sup>56,57</sup> and can reduce the loss of carbon as CH<sub>4</sub> by formation of alkylated aromatic products. We hypothesize that the increase in the presence of Brønsted acid sites with an increase in loading leads to the observed increase in alkylation rates (Figure 5). Taken together, the combined reactivity and characterization data suggest that as the coverage of Mo approaches a monolayer, the prevalence of

oligomeric species increases, which results in higher HDO and alkylation activity. Beyond a monolayer, the overall activity decreases because the presence of bulk MoO<sub>3</sub> and Zr(MoO<sub>4</sub>)<sub>2</sub> crystallites decreases the total number of HDO-active species, but the activity per site is no longer altered for HDO.

Our previous study established that the nature of the support influences the reducibility and prevalence of reduced oxidation states of Mo (Mo<sup>5+</sup> and Mo<sup>3+</sup>).<sup>22</sup> Post-reaction XPS showed the highest degree of reduction at the highest loadings (25 and 36 wt %), consistent with our PXRD. In the sub-monolayer coverage regime (1–15 wt %), dispersed MoO<sub>x</sub> domains are resistant to over-reduction, as seen by the higher prevalence of Mo<sup>5+</sup> species. The crucial role played by Mo<sup>5+</sup> species can be seen by the decrease in the specific HDO reactivity at loadings of ≥15 wt % corresponding to a reduction in the proportion of Mo<sup>5+</sup> species and percent redox-active Mo species. However, the nature of MoO<sub>x</sub> as isolated or oligomeric species seems to influence the reactivity the most.

## CONCLUSION

In summary, the effect of loading on the structure and reactivity of Mo species toward HDO of anisole was investigated. With an increase in the loading of MoO<sub>3</sub> from 1 to 36 wt %, dispersion of Mo varies from isolated species to oligomeric domains to finally crystallites of MoO<sub>3</sub> and Zr(MoO<sub>4</sub>)<sub>2</sub>. The specific reactivity toward HDO products benzene, and alkylated aromatics on a MoO<sub>3</sub> mass basis, increased until a monolayer dispersion of MoO<sub>x</sub> was achieved, followed by a decrease, as crystallites of MoO<sub>3</sub> and Zr(MoO<sub>4</sub>)<sub>2</sub> phases were formed. Normalization by data from oxygen chemisorption reveals that the difference in HDO reactivity is due to the nature of dispersed MoO<sub>x</sub> species. Isolated MoO<sub>x</sub> domains are less reducible and reactive towards HDO than oligomeric domains, as shown by H<sub>2</sub>-TPR. Once a monolayer coverage is achieved, a higher loading of MoO<sub>3</sub> yields no significant increase in intrinsic HDO reactivity. A similar trend was observed for alkylation rates and linked to the nature of MoO<sub>x</sub> species and their reducibility. At the highest loadings (25 and 36 wt %), the MoO<sub>3</sub> crystallites undergo over-reduction to MoO<sub>2</sub>, while at sub-monolayer coverages, ZrO<sub>2</sub> can stabilize the Mo<sup>5+</sup> species. The reducibility and nature of dispersed MoO<sub>x</sub> species have been shown to influence reactivity toward HDO and alkylation. Overall, the dispersion of oligomeric MoO<sub>x</sub> species achieved at loadings approaching a monolayer coverage (~5 Mo/nm<sup>2</sup>) is most reactive toward HDO and alkylation.

## ASSOCIATED CONTENT

### Supporting Information

The Supporting Information is available free of charge on the ACS Publications website at DOI: 10.1021/acssuschemeng.7b00642.

Catalyst preparation, characterization, and additional figures referenced in the text (PDF)

## AUTHOR INFORMATION

### Corresponding Author

\*E-mail: yroman@mit.edu. Phone: (+1) 617-253-7090.

### ORCID

Yuri Román-Leshkov: 0000-0002-0025-4233

## Funding

This research was funded by BP through the Massachusetts Institute of Technology Energy Initiative Advanced Conversion Research Program (Grant 1454299).

## Notes

The authors declare no competing financial interest.

## ACKNOWLEDGMENTS

The authors thank the Institute of Soldier Nanotechnologies at the Massachusetts Institute of Technology (MIT) for access to the Horiba Raman microscope. The authors also acknowledge the Center of Materials Science and Engineering (CMSE) at MIT for access to PHI Versaprobe II and Cary 5000 (Varian) instruments for X-ray photoelectron spectroscopy and DRUV spectroscopy, respectively.

## REFERENCES

- Huber, G. W.; Corma, A. Synergies between Bio- and Oil Refineries for the Production of Fuels from Biomass. *Angew. Chem., Int. Ed.* **2007**, *46*, 7184–7201.
- Huber, G. W.; Iborra, S.; Corma, A. Synthesis of Transportation Fuels from Biomass: Chemistry, Catalysts, and Engineering. *Chem. Rev.* **2006**, *106*, 4044–4098.
- Czernik, S.; Bridgwater, A. V. Overview of Applications of Biomass Fast Pyrolysis Oil. *Energy Fuels* **2004**, *18*, 590–598.
- Zhang, Q.; Chang, J.; Wang, T.; Xu, Y. Review of Biomass Pyrolysis Oil Properties and Upgrading Research. *Energy Convers. Manage.* **2007**, *48*, 87–92.
- Bu, Q.; Lei, H.; Zacher, A. H.; Wang, L.; Ren, S.; Liang, J.; Wei, Y.; Liu, Y.; Tang, J.; Zhang, Q.; Ruan, R. A Review of Catalytic Hydrodeoxygenation of Lignin-Derived Phenols from Biomass Pyrolysis. *Bioresour. Technol.* **2012**, *124*, 470–477.
- Furimsky, E. Hydroprocessing Challenges in Biofuels Production. *Catal. Today* **2013**, *217*, 13–56.
- Wang, H.; Male, J.; Wang, Y. Recent Advances in Hydrotreating of Pyrolysis Bio-Oil and Its Oxygen-Containing Model Compounds. *ACS Catal.* **2013**, *3*, 1047–1070.
- Saidi, M.; Samimi, F.; Karimipourfard, D.; Nimmanwudipong, T.; Gates, B. C.; Rahimpour, M. R. Upgrading of Lignin-Derived Bio-Oils by Catalytic Hydrodeoxygenation. *Energy Environ. Sci.* **2014**, *7*, 103–129.
- Schutyser, W.; Van den Bosch, S.; Renders, T.; De Boe, T.; Koelewijn, S. F.; Dewaele, A.; Ennaert, T.; Verkinderen, O.; Goderis, B.; Courtin, C. M.; Sels, B. F. Influence of Bio-Based Solvents on the Catalytic Reductive Fractionation of Birch Wood. *Green Chem.* **2015**, *17*, 5035–5045.
- Van den Bosch, S.; Schutyser, W.; Koelewijn, S. F.; Renders, T.; Courtin, C. M.; Sels, B. F. Tuning the Lignin Oil OH-Content with Ru and Pd Catalysts During Lignin Hydrogenolysis on Birch Wood. *Chem. Commun.* **2015**, *51*, 13158–13161.
- Van den Bosch, S.; Schutyser, W.; Vanholme, R.; Driessen, T.; Koelewijn, S. F.; Renders, T.; De Meester, B.; Huijgen, W. J. J.; Dehaen, W.; Courtin, C. M.; Lagrain, B.; Boerjan, W.; Sels, B. F. Reductive Lignocellulose Fractionation into Soluble Lignin-Derived Phenolic Monomers and Dimers and Processable Carbohydrate Pulp. *Energy Environ. Sci.* **2015**, *8*, 1748–1763.
- Anderson, E. M.; Katahira, R.; Reed, M.; Resch, M. G.; Karp, E. M.; Beckham, G. T.; Román-Leshkov, Y. Reductive Catalytic Fractionation of Corn Stover Lignin. *ACS Sustainable Chem. Eng.* **2016**, *4*, 6940–6950.
- Verboekend, D.; Liao, Y. H.; Schutyser, W.; Sels, B. F. Alkylphenols to Phenol and Olefins by Zeolite Catalysis: A Pathway to Valorize Raw and Fossilized Lignocellulose. *Green Chem.* **2016**, *18*, 297–306.
- Jin, S. H.; Xiao, Z. H.; Li, C.; Chen, X.; Wang, L.; Xing, J. C.; Li, W. Z.; Liang, C. H. Catalytic Hydrodeoxygenation of Anisole as Lignin Model Compound over Supported Nickel Catalysts. *Catal. Today* **2014**, *234*, 125–132.
- Jin, S. H.; Xiao, Z. H.; Chen, X.; Wang, L.; Guo, J.; Zhang, M.; Liang, C. H. Cleavage of Lignin-Derived 4-O-5 Aryl Ethers over Nickel Nanoparticles Supported on Niobic Acid-Activated Carbon Composites. *Ind. Eng. Chem. Res.* **2015**, *54*, 2302–2310.
- Mukarakate, C.; Watson, M. J.; ten Dam, J.; Baucherel, X.; Budhi, S.; Yung, M. M.; Ben, H. X.; Iisa, K.; Baldwin, R. M.; Nimlos, M. R. Upgrading Biomass Pyrolysis Vapors over Beta-Zeolites: Role of Silica-to-Alumina Ratio. *Green Chem.* **2014**, *16*, 4891–4905.
- Iisa, K.; French, R. J.; Orton, K. A.; Budhi, S.; Mukarakate, C.; Stanton, A. R.; Yung, M. M.; Nimlos, M. R. Catalytic Pyrolysis of Pine over HZSM-5 with Different Binders. *Top. Catal.* **2016**, *59*, 94–108.
- Zhang, H. Y.; Cheng, Y. T.; Vispute, T. P.; Xiao, R.; Huber, G. W. Catalytic Conversion of Biomass-Derived Feedstocks into Olefins and Aromatics with ZSM-5: The Hydrogen to Carbon Effective Ratio. *Energy Environ. Sci.* **2011**, *4*, 2297–2307.
- Persson, N. E.; Blass, S. D.; Rosenthal, C.; Bhan, A.; Schmidt, L. D. On-Line Deoxygenation of Cellulose Pyrolysis Vapors in a Staged Autothermal Reactor. *RSC Adv.* **2013**, *3*, 20163–20170.
- Prasomsri, T.; Nimmanwudipong, T.; Roman-Leshkov, Y. Effective Hydrodeoxygenation of Biomass-Derived Oxygenates into Unsaturated Hydrocarbons by MoO<sub>3</sub> Using Low H<sub>2</sub> Pressures. *Energy Environ. Sci.* **2013**, *6*, 1732–1738.
- Prasomsri, T.; Shetty, M.; Murugappan, K.; Román-Leshkov, Y. Insights into the Catalytic Activity and Surface Modification of MoO<sub>3</sub> During the Hydrodeoxygenation of Lignin-Derived Model Compounds into Aromatic Hydrocarbons under Low Hydrogen Pressures. *Energy Environ. Sci.* **2014**, *7*, 2660–2669.
- Shetty, M.; Murugappan, K.; Prasomsri, T.; Green, W. H.; Roman-Leshkov, Y. Reactivity and Stability Investigation of Supported Molybdenum Oxide Catalysts for the Hydrodeoxygenation (HDO) of m-cresol. *J. Catal.* **2015**, *331*, 86–97.
- Budhi, S.; Mukarakate, C.; Iisa, K.; Pylypenko, S.; Ciesielski, P. N.; Yung, M. M.; Donohoe, B. S.; Katahira, R.; Nimlos, M. R.; Trewyn, B. G. Molybdenum Incorporated Mesoporous Silica Catalyst for Production of Biofuels and Value-Added Chemicals Via Catalytic Fast Pyrolysis. *Green Chem.* **2015**, *17*, 3035–3046.
- Murugappan, K.; Mukarakate, C.; Budhi, S.; Shetty, M.; Nimlos, M. R.; Román-Leshkov, Y. Supported Molybdenum Oxides as Effective Catalysts for the Catalytic Fast Pyrolysis of Lignocellulosic Biomass. *Green Chem.* **2016**, *18*, 5548–5557.
- Nolte, M. W.; Zhang, J.; Shanks, B. H. Ex Situ Hydrodeoxygenation in Biomass Pyrolysis Using Molybdenum Oxide and Low Pressure Hydrogen. *Green Chem.* **2016**, *18*, 134–138.
- Zhou, G.; Jensen, P. A.; Le, D. M.; Knudsen, N. O.; Jensen, A. D. Atmospheric Hydrodeoxygenation of Biomass Fast Pyrolysis Vapor by MoO<sub>3</sub>. *ACS Sustainable Chem. Eng.* **2016**, *4*, 5432–5440.
- Hu, H. C.; Wachs, I. E. Catalytic Properties of Supported Molybdenum Oxide Catalysts - in-situ Raman and Methanol Oxidation Studies. *J. Phys. Chem.* **1995**, *99*, 10911–10922.
- Chen, K.; Xie, S.; Bell, A. T.; Iglesia, E. Structure and Properties of Oxidative Dehydrogenation Catalysts Based on MoO<sub>3</sub>/Al<sub>2</sub>O<sub>3</sub>. *J. Catal.* **2001**, *198*, 232–242.
- Liu, H. C.; Cheung, P.; Iglesia, E. Zirconia-Supported MoO<sub>x</sub> Catalysts for the Selective Oxidation of Dimethyl Ether to Formaldehyde: Structure, Redox Properties, and Reaction Pathways. *J. Phys. Chem. B* **2003**, *107*, 4118–4127.
- Brunauer, S.; Emmett, P. H.; Teller, E. Adsorption of Gases in Multimolecular Layers. *J. Am. Chem. Soc.* **1938**, *60*, 309–319.
- Xie, S. B.; Chen, K. D.; Bell, A. T.; Iglesia, E. Structural Characterization of Molybdenum Oxide Supported on Zirconia. *J. Phys. Chem. B* **2000**, *104*, 10059–10068.
- Samaranch, B.; Ramírez de la Piscina, P.; Clet, G.; Houalla, M.; Homs, N. Study of the Structure, Acidic, and Catalytic Properties of Binary Mixed-Oxide MoO<sub>3</sub>-ZrO<sub>2</sub> Systems. *Chem. Mater.* **2006**, *18*, 1581–1586.



- (33) Calafat, A.; Avilan, L.; Aldana, J. The Influence of Preparation Conditions on the Surface Area and Phase Formation of MoO<sub>3</sub>/ZrO<sub>2</sub> Catalysts. *Appl. Catal., A* **2000**, *201*, 215–223.
- (34) Liu, H.; Cheung, P.; Iglesia, E. Structure and Support Effects on the Selective Oxidation of Dimethyl Ether to Formaldehyde Catalyzed by MoO<sub>x</sub> Domains. *J. Catal.* **2003**, *217*, 222–232.
- (35) Shupyk, I.; Piquemal, J. Y.; Briot, E.; Vaulay, M. J.; Connan, C.; Truong, S.; Zaitsev, V.; Bozon-Verduraz, F. The Use of Low-Nuclearity Oxoperoxo Molybdenum Species to Achieve High Dispersions on Zirconia Materials. *Appl. Catal., A* **2007**, *325*, 140–153.
- (36) Miyata, H.; Tokuda, S.; Ono, T.; Ohno, T.; Hatayama, F. Infrared, Laser-Raman and X-Ray-Diffraction Investigation of MoO<sub>3</sub>/ZrO<sub>2</sub> and the Oxidation of (Z)-but-2-ene. *J. Chem. Soc., Faraday Trans.* **1990**, *86*, 2291–2295.
- (37) Chen, K. D.; Xie, S. B.; Iglesia, E.; Bell, A. T. Structure and Properties of Zirconia-Supported Molybdenum Oxide Catalysts for Oxidative Dehydrogenation of Propane. *J. Catal.* **2000**, *189*, 421–430.
- (38) Radhakrishnan, R.; Reed, C.; Oyama, S. T.; Seman, M.; Kondo, J. N.; Domen, K.; Ohminami, Y.; Asakura, K. Variability in the Structure of Supported MoO<sub>3</sub> Catalysts: Studies Using Raman and X-Ray Absorption Spectroscopy with Ab Initio Calculations. *J. Phys. Chem. B* **2001**, *105*, 8519–8530.
- (39) Bhaskar, T.; Reddy, K. R.; Kumar, C. P.; Murthy, M. R. V. S.; Chary, K. V. R. Characterization and Reactivity of Molybdenum Oxide Catalysts Supported on Zirconia. *Appl. Catal., A* **2001**, *211*, 189–201.
- (40) Chary, K. V. R.; Bhaskar, T.; Kishan, G.; Reddy, K. R. Characterization and Reactivity of Molybdenum Oxide Catalysts Supported on Niobia. *J. Phys. Chem. B* **2001**, *105*, 4392–4399.
- (41) Chary, K. V. R.; Reddy, K. R.; Kishan, G.; Niemantsverdriet, J. W.; Mestl, G. Structure and Catalytic Properties of Molybdenum Oxide Catalysts Supported on Zirconia. *J. Catal.* **2004**, *226*, 283–291.
- (42) Cui, Y.; Liu, N.; Xia, Y.; Lv, J.; Zheng, S.; Xue, N.; Peng, L.; Guo, X.; Ding, W. Efficient Self-Metathesis of 1-Butene on Molybdenum Oxide Supported on Silica Modified One-Dimensional  $\gamma$ -Al<sub>2</sub>O<sub>3</sub>. *J. Mol. Catal. A: Chem.* **2014**, *394*, 1–9.
- (43) Barton, D. G.; Shtein, M.; Wilson, R. D.; Soled, S. L.; Iglesia, E. Structure and Electronic Properties of Solid Acids Based on Tungsten Oxide Nanostructures. *J. Phys. Chem. B* **1999**, *103*, 630–640.
- (44) Barton, D. G.; Soled, S. L.; Meitzner, G. D.; Fuentes, G. A.; Iglesia, E. Structural and Catalytic Characterization of Solid Acids Based on Zirconia Modified by Tungsten Oxide. *J. Catal.* **1999**, *181*, 57–72.
- (45) Regalbuto, J. R.; Ha, J. W. A Corrected Procedure and Consistent Interpretation for Temperature-Programmed Reduction of Supported MoO<sub>3</sub>. *Catal. Lett.* **1994**, *29*, 189–207.
- (46) Abello, M. C.; Gomez, M. F.; Ferretti, O. Mo/ $\gamma$ -Al<sub>2</sub>O<sub>3</sub> Catalysts for the Oxidative Dehydrogenation of Propane. Effect of Mo Loading. *Appl. Catal., A* **2001**, *207*, 421–431.
- (47) Chen, K.; Bell, A. T.; Iglesia, E. The Relationship between the Electronic and Redox Properties of Dispersed Metal Oxides and Their Turnover Rates in Oxidative Dehydrogenation Reactions. *J. Catal.* **2002**, *209*, 35–42.
- (48) Kumar, M.; Aberuagba, F.; Gupta, J. K.; Rawat, K. S.; Sharma, L. D.; Murali Dhar, G. Temperature-Programmed Reduction and Acidic Properties of Molybdenum Supports on MgO-Al<sub>2</sub>O<sub>3</sub> and Their Correlation with Catalytic Activity. *J. Mol. Catal. A: Chem.* **2004**, *213*, 217–223.
- (49) Choi, J.-G.; Thompson, L. XPS Study of as-Prepared and Reduced Molybdenum Oxides. *Appl. Surf. Sci.* **1996**, *93*, 143–149.
- (50) El-Sharkawy, E. A.; Khder, A. S.; Ahmed, A. I. Structural Characterization and Catalytic Activity of Molybdenum Oxide Supported Zirconia Catalysts. *Microporous Mesoporous Mater.* **2007**, *102*, 128–137.
- (51) Barton, D. G.; Soled, S. L.; Iglesia, E. Solid Acid Catalysts Based on Supported Tungsten Oxides. *Top. Catal.* **1998**, *6*, 87–99.
- (52) Wachs, I. E. Raman and IR Studies of Surface Metal Oxide Species on Oxide Supports: Supported Metal Oxide Catalysts. *Catal. Today* **1996**, *27*, 437–455.
- (53) Onfroy, T.; Clet, G.; Houalla, M. Acidity, Surface Structure, and Catalytic Performance of WO<sub>x</sub> Supported on Monoclinic Zirconia. *J. Phys. Chem. B* **2005**, *109*, 3345–3354.
- (54) Xu, J.; Zheng, A. M.; Yang, J.; Su, Y. C.; Wang, J. Q.; Zeng, D. L.; Zhang, M. J.; Ye, C. H.; Deng, F. Acidity of Mesoporous MoO<sub>x</sub>/ZrO<sub>2</sub> and WO<sub>x</sub>/ZrO<sub>2</sub> Materials: A Combined Solid-State NMR and Theoretical Calculation Study. *J. Phys. Chem. B* **2006**, *110*, 10662–10671.
- (55) Yori, J. C.; Pieck, C. L.; Parera, J. M. Alkane Isomerization on MoO<sub>3</sub>/ZrO<sub>2</sub> Catalysts. *Catal. Lett.* **2000**, *64*, 141–146.
- (56) Bellussi, G.; Pazzuconi, G.; Perego, C.; Girotti, G.; Terzoni, G. Liquid-Phase Alkylation of Benzene with Light Olefins Catalyzed by Beta-Zeolites. *J. Catal.* **1995**, *157*, 227–234.
- (57) Bellussi, G.; Pazzuconi, G.; Perego, C.; Girotti, G.; Terzoni, G. Liquid-Phase Alkylation of Benzene with Light Olefins Catalyzed by Beta Zeolites. *J. Catal.* **1996**, *158*, 361.